Naval Research Laboratory

Washington, DC 20375-5320

NRL/MR/5650--15-9626

Investigation of Analog Photonic Link Technology for Timing and Metrological Applications

Vincent J. Urick
Meredith N. Hutchinson
Ross T. Schermer

Photonics Technology Branch
Optical Sciences Division

May 18, 2015

REPORT DOCUMENTATION PAGE

Form Approved
OMB No. 0704-0188

1. REPORT DATE *(DD-MM-YYYY)*	**2. REPORT TYPE**	**3. DATES COVERED** *(From - To)*
18-05-2015	Memorandum	01 October 2014 – 19 March 2015

4. TITLE AND SUBTITLE

Investigation of Analog Photonic Link Technology for Timing and Metrological Applications

5a. CONTRACT NUMBER

5b. GRANT NUMBER

5c. PROGRAM ELEMENT NUMBER

6. AUTHOR(S)

Vincent J. Urick, Meredith N. Hutchinson, and Ross T. Schermer

5d. PROJECT NUMBER

5e. TASK NUMBER

5f. WORK UNIT NUMBER
4973

7. PERFORMING ORGANIZATION NAME(S) AND ADDRESS(ES)

Naval Research Laboratory, Code 5650
4555 Overlook Avenue, SW
Washington, DC 20375-5320

8. PERFORMING ORGANIZATION REPORT NUMBER

NRL/MR/5650--15-9626

9. SPONSORING / MONITORING AGENCY NAME(S) AND ADDRESS(ES)

Office of Naval Research
One Liberty Center
875 North Randolph Street, Suite 1425
Arlington, VA 22203-1995

10. SPONSOR / MONITOR'S ACRONYM(S)

ONR

11. SPONSOR / MONITOR'S REPORT NUMBER(S)

12. DISTRIBUTION / AVAILABILITY STATEMENT

Approved for public release; distribution is unlimited.

13. SUPPLEMENTARY NOTES

14. ABSTRACT

Single-sideband phase noise measurements have been conducted in support of precision timing concepts. The various items studied include optical and electrical discrete components, short- and long-length fiber-optic signal transmission with and without optical amplification, and free-space (wireless) radio-frequency transmission with and without optical feeds. A design and associated single-sideband phase noise performance of a true-time-delay modulator based on acousto-optic beam deflection is also presented.

15. SUBJECT TERMS

Microwave photonics
RF photonics
Fiber-optic delay lines
Photodetectors
Phase noise

16. SECURITY CLASSIFICATION OF:			**17. LIMITATION OF ABSTRACT**	**18. NUMBER OF PAGES**	**19a. NAME OF RESPONSIBLE PERSON**
a. REPORT	**b. ABSTRACT**	**c. THIS PAGE**			Vincent J. Urick
Unclassified Unlimited	Unclassified Unlimited	Unclassified Unlimited	Unclassified Unlimited	22	**19b. TELEPHONE NUMBER** *(include area code)* (202) 767-9352

Standard Form 298 (Rev. 8-98)
Prescribed by ANSI Std. Z39.18

TABLE OF CONTENTS

EXECUTIVE SUMMARY

The performance of analog photonic technology and some associated RF components are measured. The primary results include:

- Single-sideband phase noise measurements with discussion pertaining to various items:
  - Optical and electrical components
  - Short- and long-length fiber-optic signal transmission with and without optical amplification
  - Free-space (wireless) radio-frequency transmission with and without optical feeds
- A design and associated single-sideband phase noise performance of a true-time-delay modulator based on acousto-optic beam deflection.

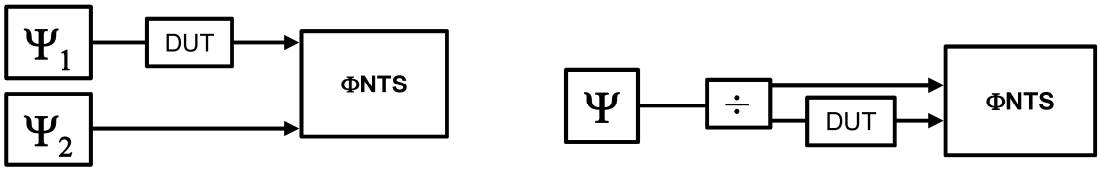

(a) (b)

Figure 1.1: Apparatus for phase noise measurements. (a) Setup using separate stimulus and reference oscillators. (b) Architecture for residual phase noise measurements. Ψ: Poseidon 10-GHz oscillator, DUT: device under test, ΦNTS: Agilent E5500A/B phase noise test set.

1 PHASE NOISE MEASUREMENTS

The majority of the measurements were conducted using the apparatus shown in Fig. 1.1. Two state-of-the-art 10 GHz oscillators (PSI SLCO-BCS) were utilized as the stimulus and reference signals. An Agilent E5500A/B phase noise test set was employed for the collection of phase noise spectra, which are reported as the single-sideband (SSB) phase noise in the radio-frequency (RF) domain, sometimes termed "script L." As shown in Fig. 1.1(a), one oscillator can be used to stimulate a device under test (DUT) and then measured against the other oscillator. This technique is adequate in the case that the DUT exhibits noise well in excess of the oscillators. Noise levels below that of the oscillator can be observed using the setup in Fig. 1.1(b), where the same oscillator is used as the reference and the stimulus. This technique is termed a residual phase noise measurement in this report.

1.1 COMPONENT-LEVEL PERFORMANCE

A critical component for this research is a basic fiber-optic link. It is sometimes misconceived that such links can impose phase noise and phase perturbations unacceptable for many applications. However, as shown in Fig. 1.2, the close-in phase noise of a standard 10-GHz fiber-optic link is well below that of the Poseidon oscillator. The fiber link in this case was a common intensity-modulation, direction-detection (IMDD) implementation with an external Mach-Zehnder modulator (see Fig. 1.11 below) operated at 8 and 30 mA average photocurrent. Also shown in Fig. 1.2 are the spectra of the absolute and residual measurements of the Poseidon oscillator. The former is state-of-the-art for electronic oscillators at 10 GHz and the latter is the noise floor for the experiment. At offset frequencies below 1 kHz, the link phase noise is considerably lower than the oscillator's. Above 10 kHz white noise floors in the links dominate and are higher than that for the oscillator. The noise floors for the links are limited by superposed shot noise, a well-understood phenomenon (see for example Chapter 3 in [1]). To further demonstrate the achievable noise level in standard fiber optic links, data for a 10-MHz test are shown in Fig. 1.3. The apparatus shown in Fig. 1.1 was not employed for collection of these data; rather an Agilent electrical spectrum analyzer with a phase noise personality (Agilent PXA N9030A) was used. Shown in Fig. 1.3 are the spectra for a 10-MHz oscillator (Wenzel 501-04609A) and the output of an IMDD link driven by the same oscillator. As can be seen, the two curves are nearly identical demonstrating that the fiber link preserves the purity of the oscillator.

Being a measurement relative to the carrier, the SSB phase noise can be strongly dependent on the RF output power. This is especially the case when a superposed white noise floor that is independent of the RF signal is the dominant factor. On the other hand, noise associated with the driving signal will typically be independent of DUT gain. Both of these cases are exemplified by the data in Fig. 1.4. As can be seen there, the phase noise below 1 kHz is independent of the RF

Manuscript approved April 1, 2015.

input power whereas the phase noise decreases with input power above 10 kHz. For the MZM input powers shown in Fig. 1.4, the MZM is not entirely linear, thus there are nonlinear trends seen in the phase noise spectra. While the precise mechanisms for all of the features are not known, it is a safe assumption that they are independent of the signal source.

The sources of phase noise in excess of shot and thermal noise for fiber-optic links are still being studied. One identified cause is the photodetector, although this area has received only minimal attention [2,3]. As an example of photodetector effects, consider the curves shown in Fig. 1.5. Shown there are residual phase noise spectra for the output of a photonic link employing a modified uni-traveling carrier (MUTC) photodiode (similar to that in [4]) at various reverse bias voltages. This MUTC photodiode has been packaged and is being considered for production; however, it is not a commercial-off-the-shelf (COTS) device. For all curves, the average photocurrent was 15 mA and a small-signal optical modulation depth was used to stimulate the photodiode. As the bias voltage is decreased, a rise in the phase noise is observed. This effect is attributed to photodiode compression but the precise physical mechanism is unknown as of yet. Different photodetectors may exhibit different phase noise characteristics. Shown in Fig. 1.6 are measured spectra for three different photodiodes under different operating conditions. The MUTC at 30 mA demonstrates the lowest phase noise. Two COTS photodiodes, Discovery Semiconductor's DSC50 and DSC50S, are also shown at 20 mA. Both have responses that are degraded at 10 GHz, with the DSC50 being more so. On the other hand, the DSC50 sources twice the RF photocurrent (four times the RF power) than the DSC50S in their linear regimes. The DSC50 exhibits less relative phase noise due to this fact, although the feature near 100 kHz may be due to compression.

Numerous RF components were measured to determine their contributions to the phase noise, namely various bias tees and RF amplifiers. The results are shown in Figs. 1.7-1.10. Shown in Fig. 1.7 are the residual phase noise spectra for four photonic links employing different biases for the photodiode circuit. As can be seen there, significant variation occurs particularly in the regime from 1-100 kHz. Therefore, judicious choice of a bias circuit can provide better performance. The data in Fig. 1.8 are for two different RF amplifiers under three RF drive powers. The low phase noise amplifier (AML 812PNB1813) is specifically designed to minimize phase noise, while the other COTS device (B&Z BZP120UD1) is a low-noise-figure design but not optimized for phase noise performance. For both amplifiers the close-in phase noise is independent of RF drive power, whereas the noise reduces with increasing power at higher offset frequencies. Two RF amplifiers later identified for certain applications were analyzed a bit more thoroughly as shown in Fig. 1.9 and 1.10. In both figures, the phase noise is shown as a function of input power to the amplifier, with the highest level being the input power at to achieve 1 dB compression of the output power. The solid lines in the figure designate the noise floor associated with the amplifier noise figure (NF). Assuming that this noise is superposed white noise, it can be calculated as –177 dBm/Hz + NF[dB] – P_{in}[dBm], where P_{in} is the input power. Shown in Fig. 1.9 are results for B&Z model BZ-02001800-302330-202020 measured relative to 10 GHz using the residual phase noise method. As seen there, the phase noise is relatively independent of RF input power expect when the white noise associated with the noise figure dominates and in the range of 10-100 MHz, where the noise floor of the measurement system comes into play. The calculated values agree closely with the measurements where applicable, with any discrepancies are within the error of the NF value. Data for a B&Z model BZY-P00010100-180827-182020 are shown in Fig. 1.10. Note that the data there are relative to 2.48832 GHz. The apparatus for these data is as shown in Fig. 1.1(b) using an Anritsu 69397B tunable source. The data in Fig. 1.10 follow trends similar to that observed in Fig. 1.9 expect at high output powers, where the noise is below the calculated values. This is attributed to changes in the amplifier performance as it approaches compression.

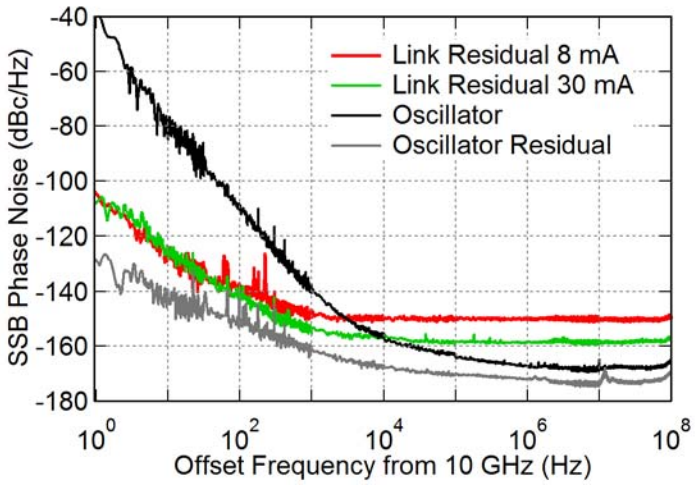

Fig. 1.2: Measured residual single-sideband (SSB) phase noise of a photonic link employing a modified uni-traveling carrier photodiode at two average currents compared to the driving oscillator. For the 8mA case no EDFA is used and the RF input power to the MZM is 12 dBm. For the 30mA case the input RF power has been increased to 19dBm and an EDFA has been added to increase the photocurrent.

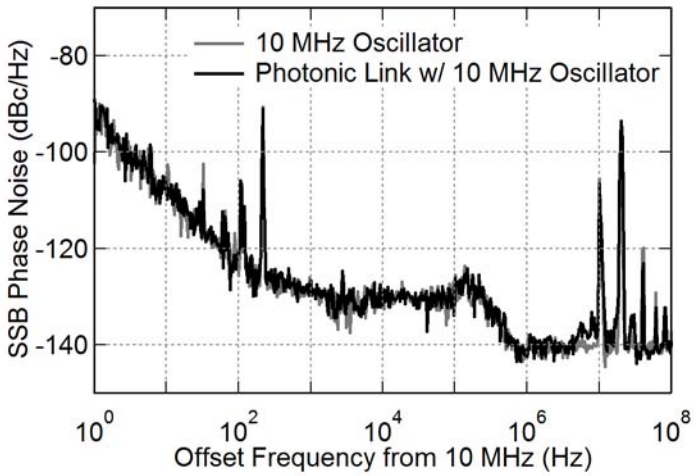

Fig. 1.3: Measured single-sideband (SSB) phase noise of a 10 MHz oscillator (gray) compared to a photonic link driven by the same 10 MHz oscillator (black).

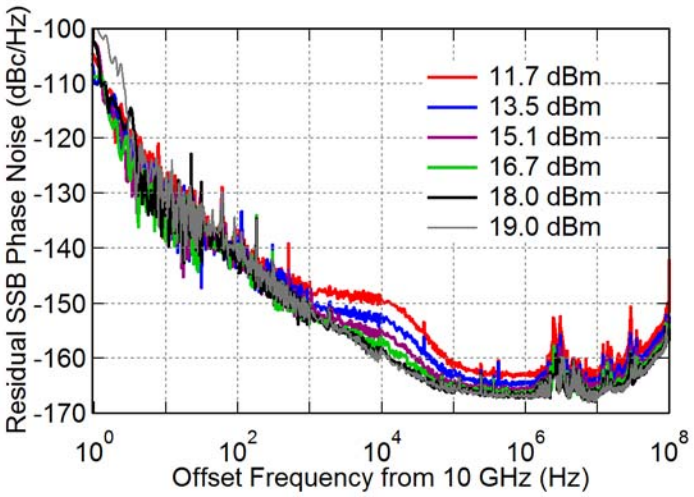

Fig. 1.4: Measured residual single-sideband (SSB) phase noise of a modified uni-traveling carrier photodiode at an average photocurrent of 20 mA with a 7 V bias for various RF input powers into the link. The phase noise is compared against a second identical modified uni-traveling carrier photodiode used as the reference.

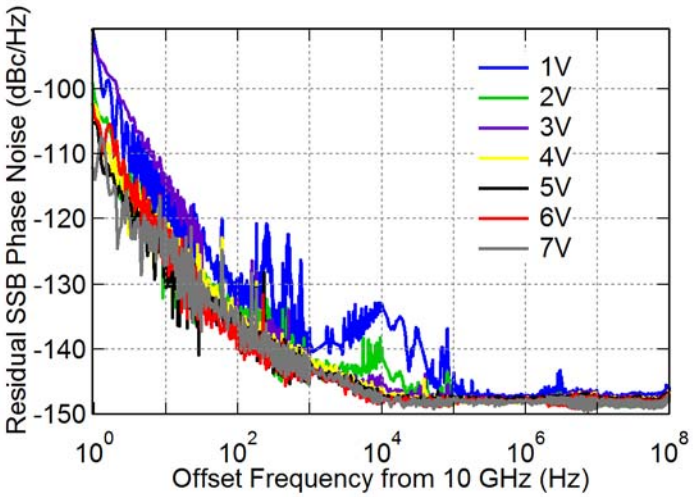

Fig. 1.5: Measured residual single-sideband (SSB) phase noise of a photonic link employing a modified uni-traveling carrier photodiode at an average photocurrent of 15 mA for various bias voltages. The phase noise is compared against a second identical modified uni-traveling carrier photodiode used as the reference.

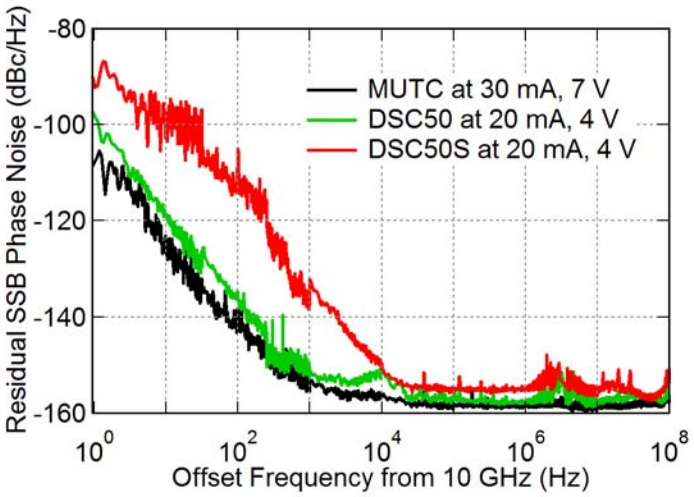

Fig. 1.6: Measured residual single-sideband (SSB) phase noise of a photonic link employing three different photodiodes.

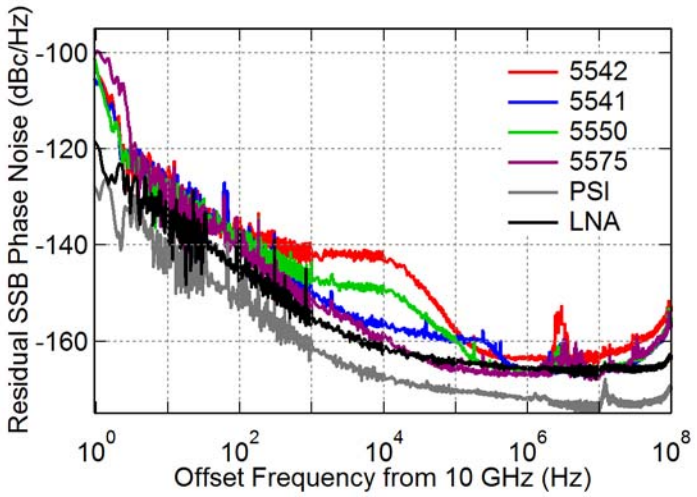

Fig. 1.7: Measured residual single-sideband (SSB) phase noise of a 10 GHz oscillator (PSI, gray) compared to that with an electronic low noise amplifier (LNA, black) and the residual phase noise of a modified uni-traveling carrier photodiode photonic using various bias tees (colored with numbers corresponding to manufacturer model numbers). Both the reference photodiode and measured photodiode employ the same model bias tee in each case.

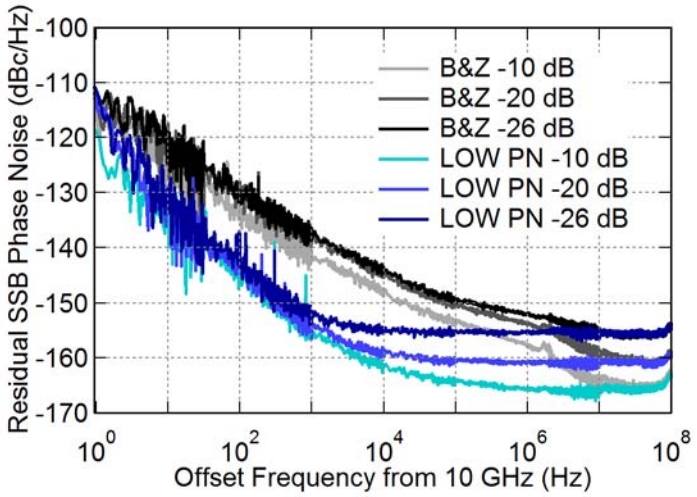

Fig. 1.8: Measured residual single-sideband (SSB) phase noise for two amplifiers with various RF pads at their inputs. The B&Z amplifier is a conventional low-noise-figure amplifier whereas the low phase noise (PN) amplifier is specially designed to minimize jitter.

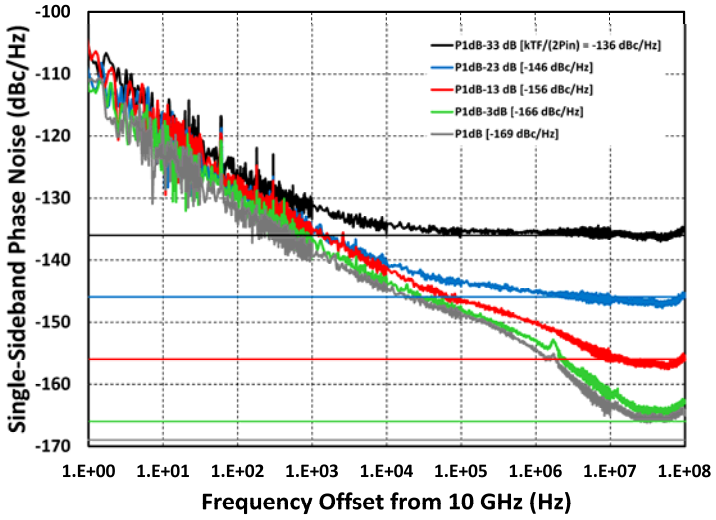

Fig. 1.9: Measured residual single-sideband (SSB) phase noise for an RF amplifier as a function of input power (P_{in}) at 10 GHz. The solid lines indicate the calculated noise floor due to the amplifier's specified noise figure NF = 2 dB (10log$F$, where F is the noise factor) and specified input power at 1-dB compression of P_{in} = –6 dBm (gray line), where k is Boltzmann's constant and T = 290 K is the standard noise temperature.

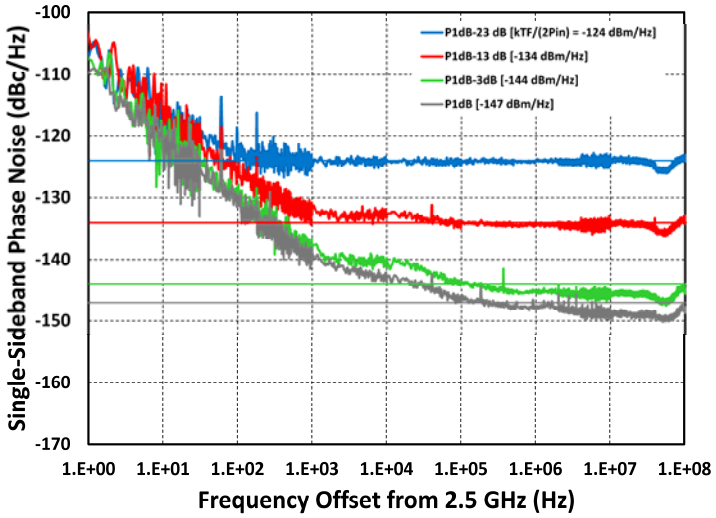

Fig. 1.10: Measured residual single-sideband (SSB) phase noise for an RF amplifier as a function of input power (P_{in}) at 10 GHz. The solid lines indicate the calculated noise floor due to the amplifier's specified noise figure NF = 1 dB (10log$F$, where F is the noise factor) and specified input power at 1-dB compression of P_{in} = –29 dBm (gray line), where k is Boltzmann's constant and T = 290 K is the standard noise temperature.

1.2 TRANSMISSION EXPERIMENTS

Numerous bench-top experiments were conducted in order to determine achievable performance levels for 10-GHz signal distribution. As described in the following two subsections, the two primary transmission medium considered were point-to-point fiber-optic links and free-space RF links. In both cases, the results presented here pertain to relatively simple laboratory environments as compared to what can quickly become very complicated scenarios for deployed systems. For example, the loss and scattering mechanisms in installed fiber-optic cabling can amount to detriments that are not easily predicted prior to installation. Similarly, the attenuation and multipath interference in wireless RF links are strong functions of weather and the surrounding environment. As appropriate, further examples will be provided in the presentation of the following data.

1.2.1 Fiber-Optic Links

All of the fiber-optic links employed for this effort utilized an IMDD architecture with an external MZM such as shown in Fig. 1.11. A laser's intensity is modulated by an RF signal via the external MZM, which converts electro-optic phase modulation into intensity modulation with an integrated Mach-Zehnder interferometer. The photodetector, often a p-i-n photodiode, converts optical intensity modulation into an electronic current, coherently reproducing the input RF signal. While these types of links are most versatile option for wideband applications, there may be value in considering other analog photonic link topologies for specific applications. For example, external phase modulation with interferometric demodulation [5] may provide some distinct advantages in single-octave systems, although RF phase noise in such optically-coherent systems should be carefully considered.

Shown in Fig. 1.12 is the diagram for the link pertaining to the data in Figs. 1.13 and 1.14. The transmission span in this case was 4 km of SMF-28, which was spooled onto a plastic reel and placed on an optical table. Shown in Fig. 1.13 are the results of measurements through the span for three received photocurrents compared to the back-to-back case (i.e. no fiber span but the photonic front- and back-end in place) at 30 mA average photocurrent. For the transmission experiments, the received photocurrent was controlled by adjusting the EDFA at the link input.

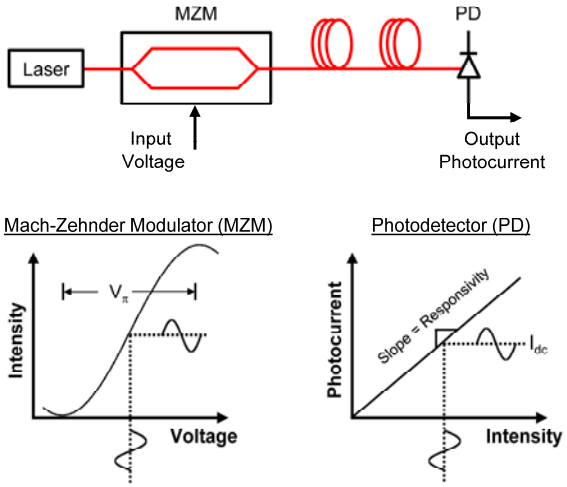

Fig. 1.11: Intensity-modulation, direct-detection link with an external MZM.

Above 1 MHz the four curves have the same noise floor. However, the 4-km links exhibit significantly more noise at lower frequency offsets, without a strong relation to average photocurrent. A notable feature is the discontinuity in the 25-mA data at 10 kHz. This is due to the slow drift in RF phase through the fiber over the residual phase noise data collection, which can take minutes, an effect that is clearly observed during the measurements. The phase-noise test set instrumentation collects data serially in bands, and sometimes adjustments are required to maintain a quadrature relationship between the two inputs to the test set [see Fig. 2.1(b)]. The variability through the fiber link is further demonstration in Fig. 1.14, where three sequential measurements at 25 mA are compared.

A second set of fiber experiments were conducted using the binary fiber-optic delay line (BiFODL) unit shown in Fig. 1.15. Contained in a rack-mount enclosure, the BiFODL was originally built for delay-line signal processing experiments but was utilized here to quickly observe the performance as a function of propagation distance. Furthermore, this unit may present a situation more representative of performance outside a laboratory environment in that it utilizes numerous electronic circuits and components that may be encountered in deployed fiber-optic networks. Examples of such circuits include (i) the MZM bias control board (YY Labs DLBC 60168) (ii) the EDFA driver (Lightwave Electronics LDTC 0520) and (iii) the control circuitry for the optical switches. The optical switches themselves, having finite isolation, present a mechanism for multipath optical interference that can cause optical phase-to-intensity noise conversion. The front end of this link entailed a semiconductor laser (EM4 EM600) and a 10-GHz MZM (EOSPACE). The photodiode was a Discovery Semiconductor DSC50S. Numerous experiments were conducted including repetitive measurements at about 3, 4, 6 and 10 km. Two representative phase noise spectra for the BiFODL experiments are shown in Fig. 1.16. As can be seen, there is considerable noise in the output spectra. The noise floor above 6 MHz is due to superposed noise arising from EDFA spontaneous emission and varies with received RF power, as expected. The noise level below 1 MHz was observed to be relatively independent of propagation length and RF output power. Possible sources of this noise include the above-mentioned electronics and perhaps laser phase-to-intensity noise conversion. The latter may not be the case because there is very little dependent on propagation length. However, the laser in this case was relatively broad (~100 kHz linewidth) and common point reflections could be the cause as opposed to length-dependent double Rayleigh scattering.

The final set of experiments employed a fix-length fiber-optic delay line (FODL) that is usually employed for radar testing [6]. A photograph of unit is shown in Fig. 1.17 along with a block diagram. Data were collected for both the 20-km and 40-km outputs. The low-phase-noise amplifier was placed at the link output, resulting in 5 dBm RF power into the phase noise test set for both cases (the level exiting the FODL is about -13 dBm). As with the other transmission experiments quadrature adjustments were required due to slow phase drifts during the course of the measurements, more so with the 40-km span. The results are shown in Fig. 1.18, where the residual SSB phase noise is plotted for the 20-km and 40-km spans. Shown for comparison are spectra obtained in 2012 [6] using the technique shown in Fig. 1.1(a). The superposed white noise (due to EDFA spontaneous emission) is nearly identical in both cases, with the slight variations attributed to differences in output power. All features observed in the residual phase noise data are repeatable and were observed during multiple measurements. Like the BiFODL, these data present a case of a system employing representative control electronics in that the unit is “turn-key” with a 120-V AC input.

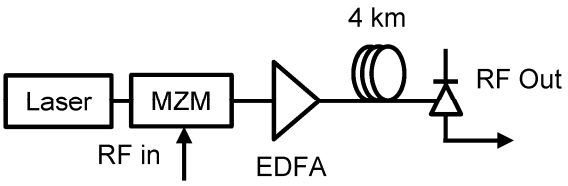

Fig. 1.12: Architecture for 4-km fiber-optic link.

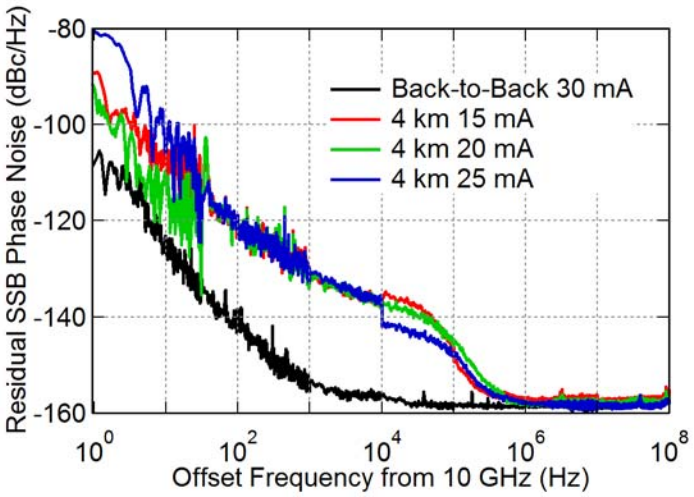

Fig. 1.13: Measured residual single-sideband (SSB) phase noise for a photonic link over 4 km of standard single mode fiber. Shown also is the back-to-back case with no significant length of fiber in place.

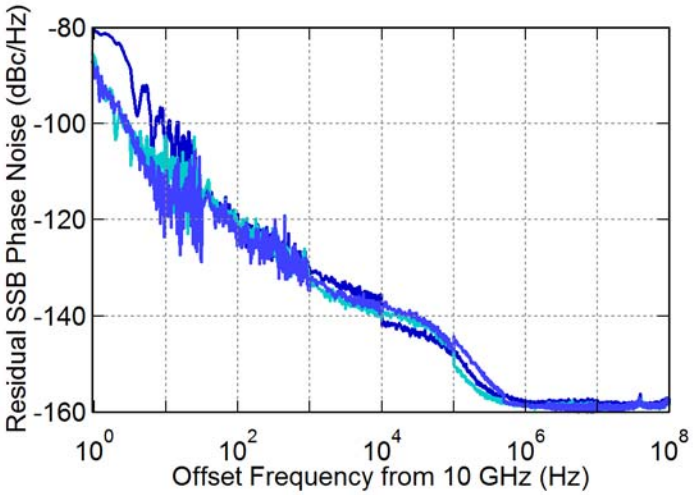

Fig. 1.14: Repeatability of measured residual single-sideband (SSB) phase noise for a 4-km fiber link at 25 mA received photocurrent. The variability due the fiber can be observed, particularly at the band breaks.

(a)

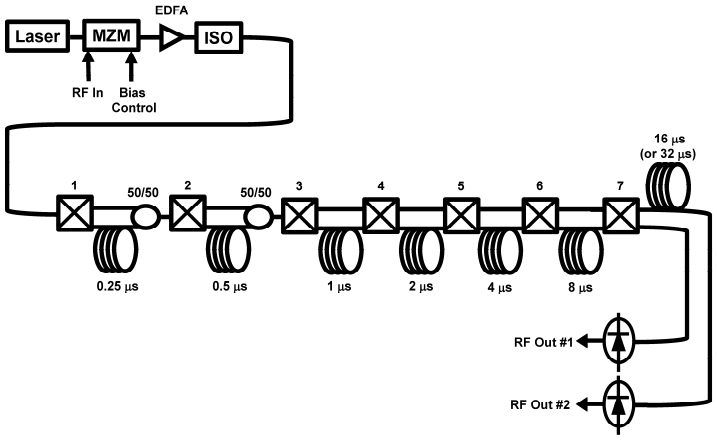

(b)

Fig. 1.15: Photograph and architecture for binary fiber-optic delay line (BiFODL).

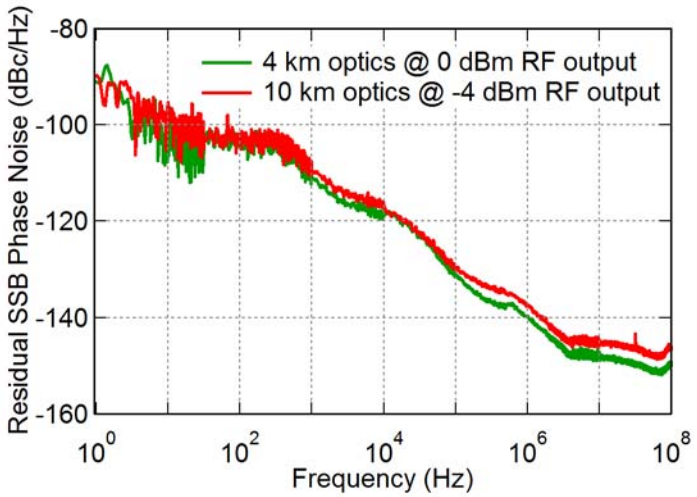

Fig. 1.16: Measurement results for the BiFODL shown in Fig. 1.13.

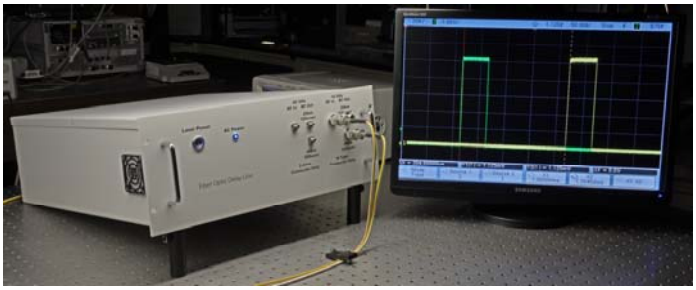

(a)

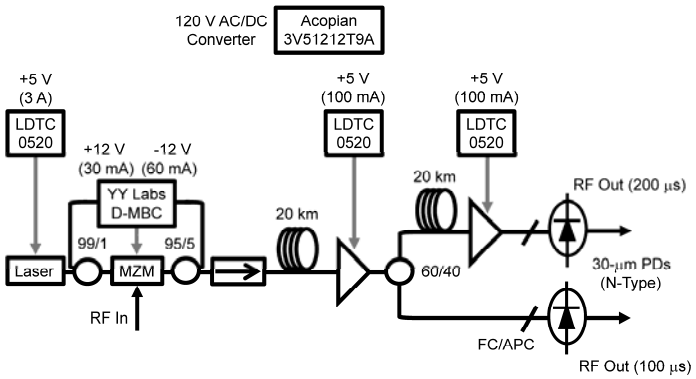

(b)

Fig. 1.17: Photograph and architecture for a fixed-length fiber-optic delay line (FODL).

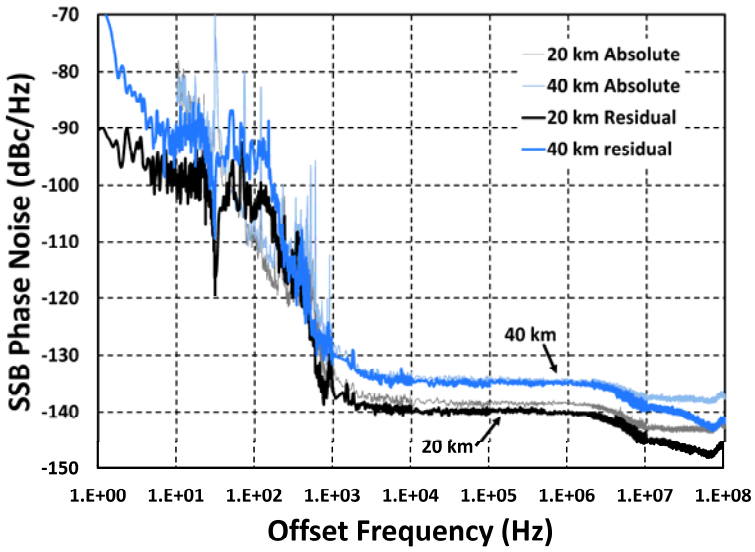

Fig. 1.18: Measurement results for the FODL shown in Fig. 1.15. For comparison, the absolute phase noise measured in late 2012 [6] is also shown.

1.2.2 Free-Space 10-GHz Links

The performance of free-space, or wireless, RF links depend on a multitude of factors. A simple bound on performance can be determined by using the Friis power transmission equation, which can be written as [9]

$$P_{\mathrm{RX}} = \frac{P_{\mathrm{TX}} G_{\mathrm{TX}} G_{\mathrm{RX}} c^2}{\left(4\pi R f\right)^2}$$

$$P_{\mathrm{RX}}\left(\mathrm{dBm}\right) = P_{\mathrm{TX}}\left(\mathrm{dBm}\right) + G_{\mathrm{TX}}\left(\mathrm{dB}\right) + G_{\mathrm{RX}}\left(\mathrm{dB}\right) - 20\log\left[f\left(\mathrm{GHz}\right)\right] - 20\log\left[R\left(\mathrm{km}\right)\right] - 92 \tag{1}$$

where P_{RX} is the average received power, P_{TX} is the transmitted power, G_{TX} is the antenna gain at the transmitter, G_{TX} is the antenna gain at the transmitter, c is the speed of light in vacuum, R is the range between antennas and f is the frequency. The second line in (1) is cast in decibel form using common units for ease of calculation. There are numerous assumptions and factors not accounted for in (1) including:

(i) It is assumed that the antennas are both aligned in polarization and to their main beams.
(ii) Multipath effects are neglected.
(iii) Antenna impedance mismatch is not accounted for.
(iv) There is no factor for atmospheric attenuation (see Fig. 1.19).

All of these issues should be considered for deployed wireless RF links.

The experiments conducted for this utilized the apparatus shown in Fig. 1.20 and variants thereof. The antennas were 2-18 GHz spirals with about unity gain (AEL ASO-1503AAT). The power amplifier was a DBS Microwave device (DB96-0611) with about 46 dB small-signal gain and a maximum output power of about 32 dBm. The LNA was the low-phase noise model used in Section 1.2.1. The results for four scenarios are shown in Fig. 1.21. First, the apparatus as shown in Fig. 1.20 with the RF power levels indicated there was measured (blue). The red curve corresponds to a measurement with the antennas replaced by a wired 45-dB attenuator, matching the measured loss through the wireless link including antenna gain. Comparison of these two curves demonstrates that the free space link adds noise at low offset frequencies. This trend is also observed when the power amplifier is fed with a photonic link having -16 dBm output power, as shown by the black and green curves.

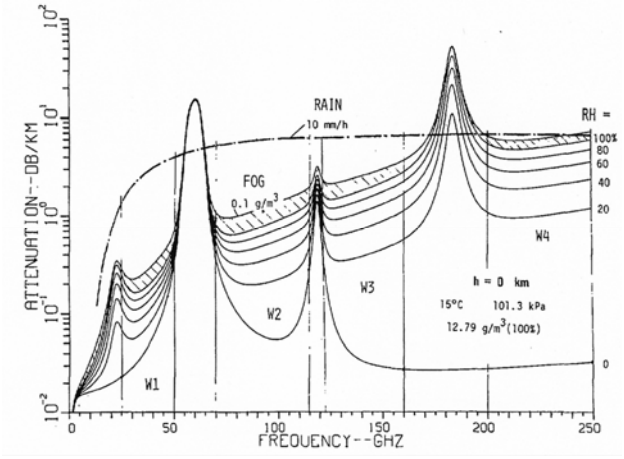

Fig. 1.19: Atmospheric attenuation at sea level for various relative humidity levels [10].

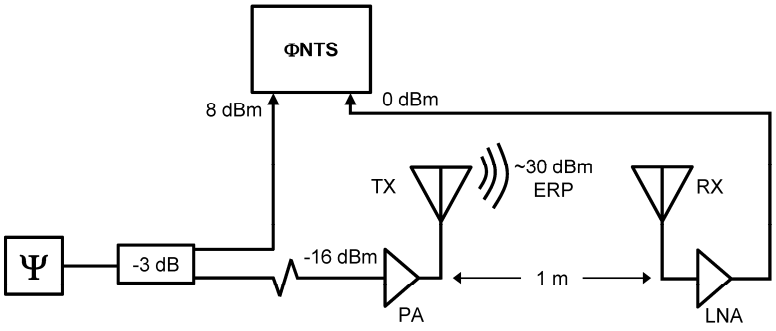

Fig. 1.20: Setup for free-space RF transmission. PA: power amplifier, LNA: low-noise amplifier, ERP: effective radiated power.

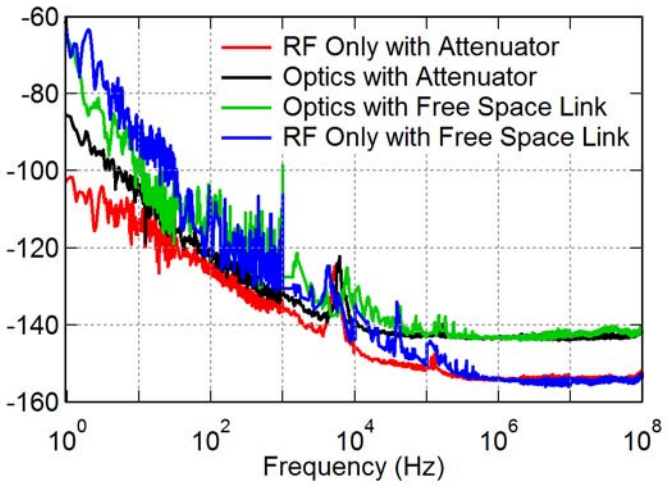

Fig. 1.21: Measurement results RF free-space link.

2 TRUE-TIME DELAY MODULATOR

The true time delay modulator utilized here is a variant on a beam-deflector design [7] using an acousto-optic modulator [8] as shown in Fig. 2.1. Changes in optical path length through the apparatus translate to true time delays (TTDs) with a basic operation as follows. An input optical signal (that can be carrying RF modulation) is passed through an optical circulator and focused into an acousto-optic (AO) cell. The AO cell is driven with a separate electronic signal that determines the beam deflection at the AO output. The deflected signal is reflected onto a tilted diffraction grating and passed backed through the device to the output. As depicted in Fig. 2.1, the TTD is achieved by varying the beam deflection and thus varying where the signal illuminates the grating.

The operation of such a TTD modulator has been detailed previously [7,8]. Here, the phase noise for a signal passing through such a device is briefly investigated. The proof-of-concept demonstration employed a lead molybdate acoustic cell with 7% diffraction efficiency at 1550 nm, which translates to high insertion loss. Note, similar acoustic cells have diffraction efficiencies upwards of 60% that can significantly reduce the optical insertion loss. The cell was driven by an Agilent 81150A arbitrary waveform generator followed by an electronic VHF amplifier with about 43 dB gain and a variable attenuator. The results of the demonstration are shown in Fig. 2.2, where residual SSB phase noise curves for three arrangements are shown. In all cases, a Poseidon oscillator at 10.24 GHz was used as the driving signal. The first (blue) was for a photonic link without the TTD modulator. This link comprised an electronic low-noise amplifier (LNA) connected to a MZM, the output of which is passed through an EDFA and then to a photodiode. An optical attenuator was then placed into the link with the same loss as the TTD modulator, an architecture that produced the red curve in Fig. 2.2. The green curve depicts the results once the TTD modulator was placed in line. As can be seen in Fig. 2.2, the TTD modulator performs about the same as the attenuated link until about 20 Hz offset frequencies. There is then considerably more noise observed to frequencies of a few hundred Hz, which is attributed to mechanical vibration in the TTD modulator apparatus. The phase noise of the TTD modulator is only slightly worse than the link with attenuator from 1 kHz to 1 MHz. The increased noise at high frequencies is attributed to the driving frequency of the AOM (40 MHz) and its harmonics. An important note is that the phase noise levels above 100 Hz shown in Fig. 2.2 are well below that for the arbitrary waveform generator specified at about -100 dBc/Hz.

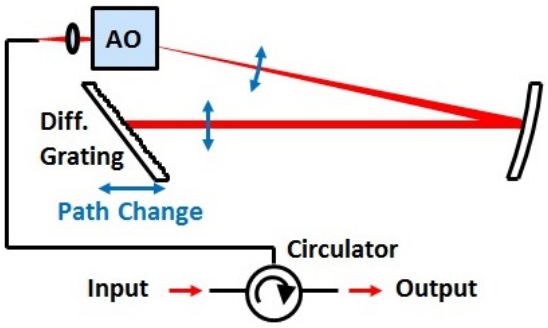

Fig. 2.1: Diagram of true-time delay modulator employing an acousto-optic (AO) cell.

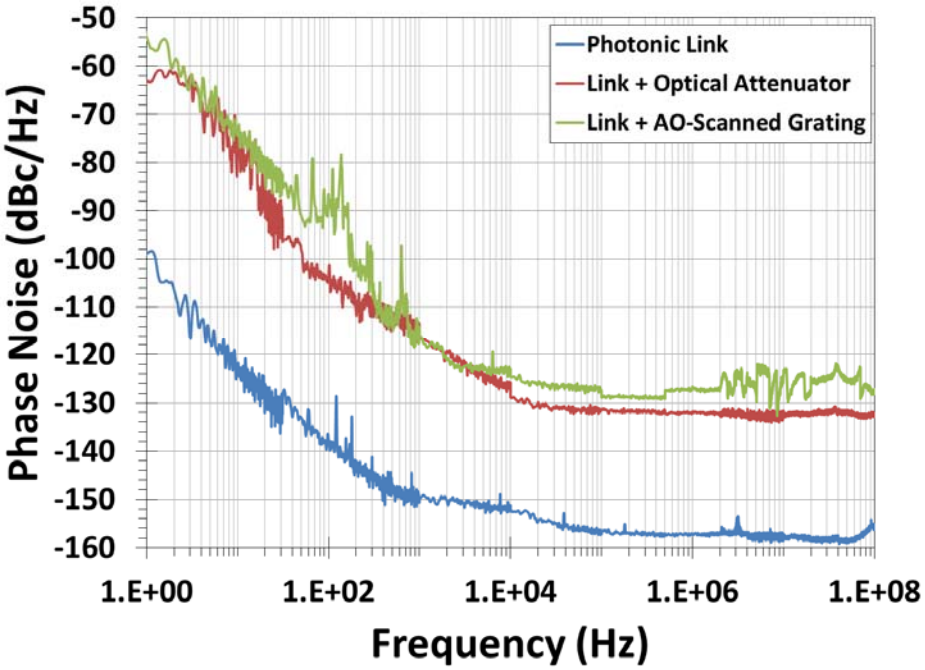

Fig. 2.2: Measured residual single-sideband phase noise in experiments at 10 GHz related to the true-time-delay modulator.

3 SUMMARY AND CONCLUSIONS

Numerous SSB phase noise measurements have been conducted on a variety of architectures and components suitable for distribution of RF signals. In general, the close-in phase noise rivals or is significantly less than that for state-of-the-art microwave oscillators. On the other hand, white noise floors at larger offset frequencies are typically higher than state-of-the-art oscillators. While these results present here may be very promising for distribution of certain signals, other factors could come into play in deployment outside a laboratory setting. For example, installed fiber-optic networks have features that could potentially increase excess phase noise. Such sources include, but are not limited to, noisey electronic circuits coupled to the optics, in-line passive and active optical components, and cabled fiber with its associated hardware. Similarly, outdoor implementations of wireless RF transmission present a complicated environments including multipath interference, other electromagnetic interference and weather-dependent effects.

The work presented here is almost entirely empirical. Some of the sources of SSB phase noise are well understood, particularly superposed noise sources that are RF-independent such as thermal noise, shot noise, signal-spontaneous noise and spontaneous-spontaneous noise. Other causes of excess phase noise have been identified such as that arising from the photodetector, fiber transmission and wireless RF transmission. However, the underlying physical mechanisms for these and other sources are not well understood. Predictive models for full scale systems could be an area of future work but would require dedication of substantial resources.

A novel TTD modulator has been adapted for phase modulation of RF signals. The SSB phase noise of a lossy prototype has been investigated and exhibited little phase noise in excess of a back-to-back comparison. Other TTD modulation mechanisms have been considered including fiber stretches (mechanical and piezoelectric), electro-optic modulators (i.e. $LiNbO_3$), electro-absorption techniques, and magneto-optic modulation.

REFERENCES

[1] V. J. Urick Jr., J. D. McKinney, and K. J. Williams, *Fundamentals of Microwave Photonics*, Wiley, 2015.

[2] J. Taylor, S. Datta, A. Hati, C. Nelson, F. Quinlan, A. Joshi, and S. Diddams, "Characterization of power-to-phase conversion in high-speed p-i-n photodiodes," *IEEE Photonics J.*, vol. 3, no. 1, pp. 140-151, Feb. 2011.

[3] D. A. Tulchinsky and K. J. Williams, "Excess amplitude and excess phase noise of RF photodiodes operated in compression," *IEEE Photonics Technol. Lett.*, vol. 17, no. 3, pp. 654-656, Mar. 2005.

[4] Z. Li, H. Pan, H. Chen, A. Beling, and J. C. Campbell, "High-saturation-current modified uni-traveling-carrier photodiode with cliff layer," IEEE J. Quantum Electron., vol. 46, no. 5, pp. 626-632, May 2010.

[5] V. J. Urick, J. D. McKinney, J. F. Diehl, and K. J. Williams, "Equations for two-tone analog optical phase modulation with an asymmetric interferometer," *IEEE Photonics Technol. Lett.*, vol. 25, no. 15, pp. 1527-1530, June 2013.

[6] V. J. Urick, J. M. Singley, C. E. Sunderman, J. F. Diehl, and K. J. Williams, "Design and performance of Ka-band fiber-optic delay lines," Naval Research Laboratory Memorandum Report, NRL/MR/5650-12-9456, Dec. 2012.

[7] R. T. Schermer, F. Bucholtz, and C. A. Villarruel, "Continuously-tunable microwave photonic true-time-delay based on a fiber-coupled beam deflector and diffraction grating," *Opt. Exp.*, vol. 19, no. 6, pp. 5371-5378, Mar. 2011.

[8] R. T. Schermer, F. Bucholtz, and C. A. Villarruel, "Microwave Photonic True-Time-Delay," U.S. Patent Application 2013/0010301 A1, 10 Jan. 2013.

[9] D. M. Pozar, Microwave Engineering, Wiley, 2011.

[10] H. J. Liebe, "Atmospheric EHF Window Transparencies near 35, 90, 140, and 220 GHz," *IEEE Trans. on Antennas and Propagation*, vol. AP-31, no. 1, pp. 127-135, 1983.